Reactivity and stability of plasma-generated oxygen and nitrogen species in buffered water solution: a computational study

Pepijn Heirman, Wilma Van Boxem, Annemie Bogaerts*

PLASMANT Research group, Department of Chemistry, University of Antwerp, Universiteitsplein 1, BE-2610 Wilrijk-Antwerp, Belgium

* annemie.bogaerts@uantwerpen.be

Supplementary Information

Contents

1. Details about the 0D model

a) Chemical kinetics model

The chemical kinetics model is based on solving a set of conservation equations (E.1) for all species included in the 0D model.

$$\frac{\partial n_s}{\partial t} = \sum_{i=1}^{j} \left[\left(a_{s,i}^{R} - a_{s,i}^{L}\right) R_i\right] \quad \text{(E.1)}$$

With n_s the density of species s (m^{-3}), j the total number of reactions, $a_{s,i}^{L}$ and $a_{s,i}^{R}$ the stoichiometric coefficients at the left and right hand side of the reaction and R_i the rate of reaction (in m^{-3}.s^{-1}), given by E.2, with k_i the rate coefficient (m^3 s^{-1} or m^6 s^{-1} for two-body or three-body reactions, respectively).

$$R_i = k_i \prod_s n_s^{\alpha_{s,i}} \quad \text{(E.2)}$$

The rate coefficients of the heavy particle reactions are either constant or dependent on the gas temperature, whereas the rate coefficients of the electron impact reactions depend on the electron temperature T_e or the reduced electric field E/N (i.e., the electric field E divided by the number density

of all neutral species N, usually expressed in Td = 10^{-21} V.m^2). The rate coefficients of the electron impact reactions are generally calculated according to equation E.3.

$$k_i = \int_{\varepsilon_{th}}^{\infty} \sigma_i(\varepsilon) v(\varepsilon) f(\varepsilon) d\varepsilon \tag{E.3}$$

With ε the electron energy (usually in eV), ε_{th} the minimum threshold energy needed to induce the reaction, $v(\varepsilon)$ the velocity of the electrons (in m s^{-1}) , $\sigma_i(\varepsilon)$ the cross section of collision i (in m^2), and $f(\varepsilon)$ the (normalized) electron energy distribution function (EEDF; in eV^{-1}) calculated using a Boltzmann solver.

In this work we solve the balance equations (E.1) of all species by means of the ZDPlaskin code[1], which also has a built-in Boltzmann solver, called BOLSIG+[2], to calculate the EEDF and the rate coefficients of the electron impact reactions based on a set of cross sections, the plasma composition, the gas temperature and the reduced electric field (E/N). The electric field (E; in V m^{-1}) is calculated from a given power density, using the so-called local field approximation[3] (E.4).

$$E = \sqrt{\frac{P}{\sigma}} \tag{E.4}$$

with P the input power density (in W.m^{-3}) and σ the plasma conductivity (A.V^{-1}.m^{-1}). The plasma conductivity is estimated at the beginning of the simulations as shown in equation E.5[3].

$$\sigma = \frac{e^2 n_{e,init}}{m_e \nu_m} \tag{E.5}$$

with e the elementary charge (1.6022x10^{-19} C), $n_{e,init}$ the initial electron density (in m^{-3}), m_e the electron mass (9.1094x10^{-31} kg) and ν_m the collision frequency (in s^{-1}) calculated using BOLSIG+. During the simulation the plasma conductivity is calculated as defined in equation E.6[3].

$$\sigma = \frac{e v_d n_e}{(\frac{E}{N})_{prev} n_0} \tag{E.6}$$

with v_d the electron drift velocity (in m.s^{-1}), which is calculated using BOLSIG+ implemented in ZDPlaskin, and $(\frac{E}{N})_{prev}$ the reduced electric field at the previous time step (in V.m^2).

b) Description of the plasma jet in the chemical kinetics model

We consider the plasma treatment of a buffered (water) solution with the kINPen. The 0D model is used for two purposes. One is to elucidate the most important species and reactions in both the gas and liquid phase. The second one is to determine the concentrations of the species at the end of the visible afterglow (i.e. 1.2 cm below the plasma jet nozzle). Both kind of information is used as input in the 2D model (see below). A cylindrical volume element is followed along the jet stream of the kINPen plasma jet using a chemical kinetics model. By doing this, a homogenous plasma along the radial axis is assumed (like a plug flow reactor). Moreover, due to the very high axial flow speed (order of 10 m.s^{-1}) compared to the radial flow speed, the axial transport of mass and energy due to drift and diffusion is neglected compared to convection. At the position where the species would reach the liquid surface, the gas phase densities are taken as input for the liquid phase module. In this liquid phase module, the concentrations of the species are determined by diffusion from gas phase species into the liquid by Henry's law, as well as by the liquid phase chemistry. This approach, which allows us to study the liquid phase concentrations using a chemical kinetics model, was introduced by Lietz and Kushner.[4] The general plasma jet set-up used in the 0D model is shown in Figure S.1.

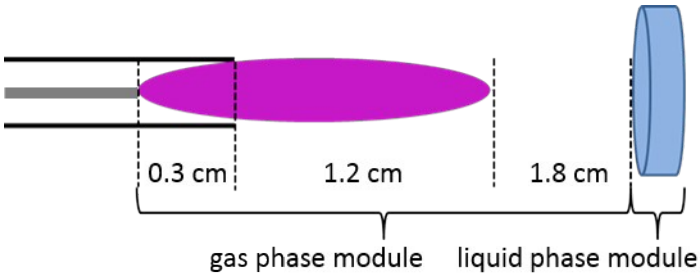

Figure S.1. *Plasma jet set-up used in the chemical kinetics model. The start of the simulation is at the end of the pin electrode (thick grey line) of the kINPen®, 3 mm before the nozzle exit. The length of the visible afterglow (purple) if 1.5 cm in total, of which 1.2 cm after the nozzle exit. The total length between the plasma jet and the liquid surface (i.e. gap) is 3 cm.*

c) Gas phase module

Conceptually, a chemical kinetics model calculates the densities of all species as a function of time (see equation E.1). However, by introducing the velocity profile of the feed gas (taken from a gas flow calculation in 2D, Figure S.2) this time can be coupled to the position along the axis, which allows us to obtain information about the species densities as a function of distance, and thus to calculate the species densities at the end of the afterglow.

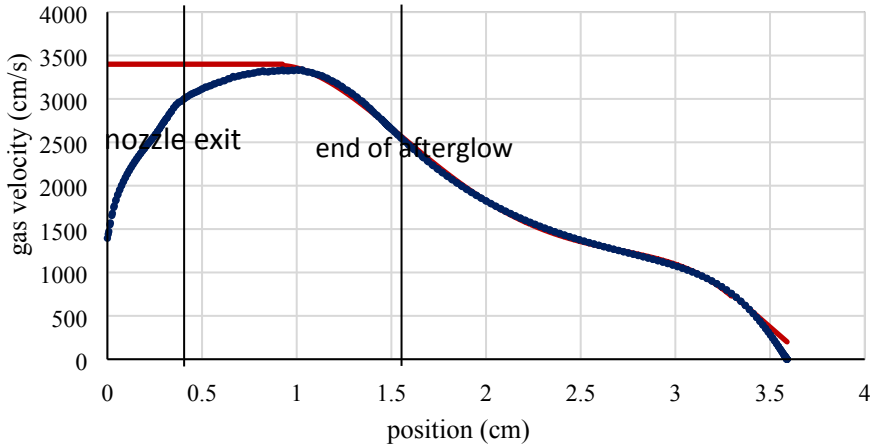

Figure S.2. *Gas velocity profile calculated in the 2D model, along the axis of the plasma jet and below the plasma jet (blue data points) and fitted curve implemented in the 0D model (red line and fit equations). Position 0 corresponds to the end of the pin electrode, 0.3 cm indicates the nozzle exit, the end of the visible afterglow is located at 1.5 cm, while 3.5 cm refers to the liquid surface. The initial increase in velocity in the 2D model is due to the presence of the pin electrode in the center of the plasma jet, but the velocity inside the plasma jet is taken as a constant value of 3400 cm.s^{-1} (the simulation only starts after the end of the pin electrode) to implement in the 0D model.*

Furthermore, as mentioned above, many of the gas phase reaction rate coefficients depend on the gas temperature. The gas temperature profile along the axis of the plasma jet is also taken from the heat transfer calculation in 2D (Figure S.3). The temperature inside the plasma jet has a constant value of 327 K[5]. Outside the plasma jet, the temperature slightly decreases, when it comes in contact with the colder ambient air (295 K). The sharp decrease in temperature in the 2D model is due to the presence of the water layer, and is not taken into account in the 0D model gas phase simulation.

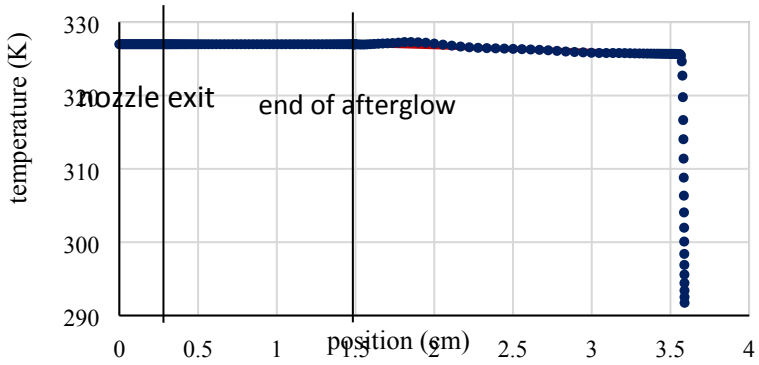

Figure S.3. *Temperature profile calculated in the 2D model (blue data points) and implemented in the 0D model (red line and fit equation). The sharp decrease in temperature in the 2D model is due to the presence of the water layer and is not implemented in the 0D model gas phase simulation. Position 0 corresponds to the end of the pin electrode, 0.3 cm indicates the nozzle exit, the end of the visible afterglow is located at 1.5 cm, while 3.5 cm refers to the liquid surface.*

Moreover, as the electron impact reactions depend on the EEDF, the reduced electric field is also required. As mentioned above, this reduced field is calculated based on the deposited power density. The maximum value of the power density is achieved at the tip of the powered electrode. Subsequently, the power density is assumed to decrease linearly along the plasma axis, reaching zero at the end of the visible plasma afterglow, which we can observe experimentally. This assumption is based on the fact that the calculated densities of the excited species quickly drop to zero when the power density drops to zero, and due to which the visible plasma plume would also be lost. The length of the visible afterglow is 1.2 cm from the nozzle exit, based on our experimental observations. The total deposited power is taken as 3.5 W, as in the experimental treatments.

Finally, the degree of mixing of ambient air with the effluent of the plasma jet will have an effect on the densities of the species. The mixing rates of O_2, N_2 and H_2O with the effluent are also calculated with the 2D model, to be correctly implemented in the 0D model (Figure S.4).

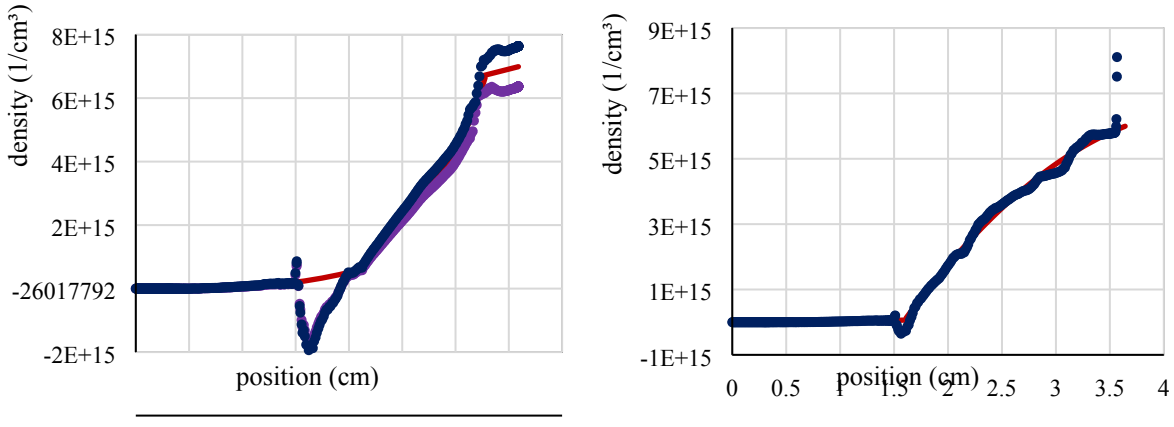

Figure S.4. *Density profiles of O_2 (left) and H_2O (right) calculated in the 2D model (blue data points). The red lines are the equations from which the derivative is implemented in the 0D model for the mixing rate as a function of position. The density profile of N_2 is similar to that of O_2, except for a higher absolute value (i.e. ca. 4 times higher, corresponding to their densities in ambient air). Position 0 corresponds to the end of the pin electrode, 0.3 cm indicates the nozzle exit, the end of the visible afterglow is located at 1.5 cm, while 3.5 cm refers to the liquid surface. The drop in concentrations at the position of 1.5 cm are due to discontinuities caused by de sharp*

boundary conditions implemented in the 2D model (i.e. from that position mixing with the ambient air is permitted). For this reason the profiles implemented in the 0D model neglect these discontinuities.

The chemistry set used for the gas phase reactions is largely taken from Murakami et al.[6] However, to include additional relevant biomedically active species (e.g. H_2O_2, HO_2, HNO_3 or HNO_2), we extended this chemistry set with the reactions describing the behaviour of these species, adopted from the chemistry set of Van Gaens and Bogaerts[7], yielding a total chemistry set of 91 different species (see Table 1 in the main paper) and 1390 reactions. The complete list of gas phase reactions implemented in the 0D model can be obtained from the authors upon request. The most important of these reactions are included in the 2D model and are listed below.

d) Liquid phase module

To investigate the chemistry occurring in the plasma-treated liquid, a second set of species and a separate chemistry set[4] were included in the chemical kinetics model. The liquid phase species were selected based on the final gas phase concentrations and their biomedical relevance. In fact, they are treated as duplicate solvated species (e.g. O_{3aq} for O_3). These aqueous species and the liquid reactions are not taken into account in the gas phase module. The species can only be transported from one to another phase through the gas-liquid interface, given by Henry's law. In general, the liquid densities of species are given by equation E.7[4]:

$$\frac{\partial n_s}{\partial t} = \sum_{i=1}^{j}\left[\left(a_{s,i}^{R} - a_{s,i}^{L}\right)R_i\right] + \frac{D_s n_{s,g}}{\Lambda^2} f_l S_{s,l} \frac{V_p}{V_l} - max\left[0, \frac{D_s(n_{s,l} - h_s n_{s,g})V_p}{\Lambda^2 \quad V_l}\right] \tag{E.7}$$

in which the first term is similar to the calculation of the gas phase species densities (conservation of mass; see above). The second term represents the diffusion of gas phase species into the liquid. In this term, D_s is the diffusion coefficient of gas phase species *s*, $n_{s,g}$ is the final gas phase density of species *s* and Λ is the diffusion length of the plasma, defined by the geometry. Furthermore, f_l is the fraction of the area of the effluent in contact with the liquid and $S_{s,l}$ is the sticking coefficient of species *s* on the liquid, given by equation E.8. More detailed information about the parameters can be found in [4].

$$S_{s,l} = \frac{h_s n_{s,g} - n_{s,l}}{h_s n_{s,g}} \tag{E.8}$$

in which h_s represents the Henry's constant of species *s*. This sticking coefficient is only used if $n_{s,l}/n_{s,g} < h_i$ and accounts for a diminishing rate of loss of the gas phase species into the liquid as the liquid density approaches its Henry's law equilibrium values. Finally, V_p and V_l represent the volume of the plasma and the liquid, respectively. The third term of equation E.7 is only non-zero if the liquid is oversaturated (i.e. if $n_{s,l}/n_{s,g} > h_i$) and represents the flux from the liquid phase into the gas phase. The Henry's constants were adopted from Lietz and Kushner[4], whereas the diffusion coefficients were taken from Verlackt et al.[8].

As mentioned before, the reaction chemistry of the liquid phase is taken from Lietz and Kushner,[4] and includes in total 43 species (Table 1 in the main paper: species in bold) and 89 reactions (Table S.1). Disproportionation reactions of HNO_2 are not included in our model, because they take place either at high temperature (100°C) or in acidic environment (or both), while we work at room temperature and in buffered solution of pH = 7.3.

With this 0D chemical kinetics approach, we are not able to simulate the bulk liquid, but only the thin interface region (just below the liquid surface). Indeed, there are spatial gradients between the liquid interface and bulk liquid, which cannot be captured in a (spatially homogeneous) 0D model. However, we only need the most important species and reactions in the liquid phase as useful information for the 2D model, which can be deduced from this 'interface region' chemistry.

Finally, it is important to mention that the liquid in our model is buffered water, with 4.8 ppm O_2 and 8.9 ppm N_2 initially dissolved into it (equilibrium values with air). The experiments were performed in

a buffered solution at pH 7.3, so the concentrations of H_3O^+ and OH^- in the liquid were fixed throughout the entire simulation at values corresponding to this pH (see details in the main paper).

Table S.1. *List of liquid phase reactions included in the liquid 0D model. The unit of the rate coefficient k is $cm^3.s^{-1}$, $cm^6.s^{-1}$, $cm^9.s^{-1}$, $cm^{12}.s^{-1}$, and $cm^{15}.s^{-1}$ for first, second, third, fourth and fifth order reactions, respectively.*

Liquid phase reactions in the 0D model	**k**
$ONOOH_{aq} + H_2O_{aq} \rightarrow H_3O^+_{aq} + ONOO^-_{aq}$	$5.0x10^{-15}$
$ONOO^-_{aq} + H_3O^+_{aq} \rightarrow H_2O_{aq} + ONOOH_{aq}$	$1.75x10^{-6}$
$HO_{2aq} + H_2O_{aq} \rightarrow H_3O^+_{aq} + O_2^-_{aq}$	$1.43x10^{-17}$
$H_3O^+_{aq} + O_2^-_{aq} \rightarrow HO_{2aq} + H_2O_{aq}$	$5.0x10^{-11}$
$HNO_{2aq} + H_2O_{aq} \rightarrow H_3O^+_{aq} + NO_2^-_{aq}$	$5.0x10^{-15}$
$H_3O^+_{aq} + NO_2^-_{aq} \rightarrow HNO_{2aq} + H_2O_{aq}$	$3.9x10^{-10}$
$HNO_{3aq} + H_2O_{aq} \rightarrow H_3O^+_{aq} + NO_3^-_{aq}$	$3.0x10^{-18}$
$H_3O^+_{aq} + NO_3^-_{aq} \rightarrow HNO_{3aq} + H_2O_{aq}$	$7.0x10^{-16}$
$HO_2NO_{2aq} + H_2O_{aq} \rightarrow O_2NO_2^-_{aq} + H_3O^+_{aq}$	$5.0x10^{-15}$
$O_2NO_2^-_{aq} + H_3O^+_{aq} \rightarrow HO_2NO_{2aq} + H_2O_{aq}$	$1.05x10^{-7}$
$OH_{aq} + H_{aq} \rightarrow H_2O_{aq}$	$3.0x10^{-11}$
$H_2O^-_{aq} + H_2O_{aq} \rightarrow H_{aq} + OH^-_{aq} + H_2O_{aq}$	$3.0x10^{-20}$
$H_2O^-_{aq} + H_{aq} \rightarrow H_{2aq} + OH^-_{aq}$	$4.0x10^{-11}$
$H_2O^-_{aq} + O_{2aq} \rightarrow H_2O_{aq} + O_2^-_{aq}$	$3.0x10^{-11}$
$H_2O^-_{aq} + OH_{aq} \rightarrow H_2O_{aq} + OH^-_{aq}$	$5.0x10^{-11}$
$H_2O^-_{aq} + H_2O_{2aq} \rightarrow H_2O_{aq} + OH^-_{aq} + OH_{aq}$	$2.0x10^{-13}$
$H_2O^-_{aq} + HO_2^-_{aq} \rightarrow OH^-_{aq} + OH^-_{aq} + OH_{aq}$	$5.0x10^{-12}$
$H_2O^-_{aq} + H_2O^-_{aq} \rightarrow H_{2aq} + OH^-_{aq} + OH^-_{aq}$	$1.0x10^{-11}$
$H_3O^+_{aq} + OH^-_{aq} \rightarrow H_2O_{aq} + H_2O_{aq}$	$5.0x10^{-15}$
$H_2O_{aq} + H_2O_{aq} \rightarrow H_3O^+_{aq} + OH^-_{aq}$	$3.02x10^{-32}$
$OH_{aq} + OH_{aq} \rightarrow H_2O_{2aq}$	$1.7x10^{-11}$
$OH_{aq} + H_{2aq} \rightarrow H_{aq} + H_2O_{aq}$	$6.0x10^{-14}$
$OH_{aq} + HO_{2aq} \rightarrow O_{2aq} + H_2O_{aq}$	$2.0x10^{-11}$
$OH_{aq} + H_2O_{2aq} \rightarrow HO_{2aq} + H_2O_{aq}$	$0.45x10^{-15}$
$OH_{aq} + O_2^-_{aq} \rightarrow O_{2aq} + OH^-_{aq}$	$1.5x10^{-11}$
$OH_{aq} + HO_2^-_{aq} \rightarrow HO_{2aq} + OH^-_{aq}$	$1.5x10^{-11}$
$OH_{aq} + NO_2^-_{aq} \rightarrow OH^-_{aq} + NO_{2aq}$	$0.3x10^{-15}$
$OH_{aq} + NO_{aq} \rightarrow HNO_{2aq}$	$3.3x10^{-11}$
$OH_{aq} + NO_{2aq} \rightarrow HNO_{3aq}$	$2.0x10^{-11}$
$OH_{aq} + HNO_{3aq} \rightarrow NO_{3aq} + H_2O_{aq}$	$2.17x10^{-15}$
$OH_{aq} + N_2O_{aq} \rightarrow HNO_{aq} + NO_{aq}$	$3.8x10^{-17}$
$H_{aq} + H_2O_{aq} \rightarrow H_{2aq} + OH_{aq}$	$1.5x10^{-21}$
$H_{aq} + H_{aq} \rightarrow H_{2aq}$	$1.5x10^{-11}$
$H_{aq} + OH^-_{aq} \rightarrow H_2O^-_{aq}$	$3.0x10^{-14}$
$H_{aq} + HO_{2aq} \rightarrow H_2O_{2aq}$	$3.0x10^{-11}$
$H_{aq} + H_2O_{2aq} \rightarrow H_2O_{aq} + OH_{aq}$	$1.5x10^{-15}$
$H_{aq} + HNO_{aq} \rightarrow OH_{aq} + NH_{aq}$	$2.18x10^{-22}$
$H_{aq} + OH^-_{aq} \rightarrow e^-_{aq} + H_2O_{aq}$	$2.0x10^{-14}$
$H_{aq} + NO_2^-_{aq} \rightarrow NO_{aq} + OH^-_{aq}$	$7.5x10^{-15}$
$H_{aq} + HNO_{2aq} \rightarrow NO_{aq} + H_2O_{aq}$	$3.52x10^{-14}$
$H_{2aq} + H_2O_{2aq} \rightarrow H_{aq} + OH_{aq} + H_2O_{aq}$	$1.0x10^{-14}$
$O_{aq} + H_2O_{aq} \rightarrow OH_{aq} + OH_{aq}$	$2.2x10^{-17}$
$O_{aq} + O_{2aq} \rightarrow O_{3aq}$	$5.0x10^{-12}$
$O_{2aq} + H_{aq} \rightarrow HO_{2aq}$	$5.0x10^{-11}$

$O_2(a^1\Delta_g)_{aq} + H_2O_{aq} \rightarrow O_{2aq} + H_2O_{aq}$	$5.0x10^{-15}$
$O_2^-{}_{aq} + HO_{2aq} + H_2O_{aq} \rightarrow O_{2aq} + H_2O_{2aq} + OH^-{}_{aq}$	$2.68x10^{-34}$
$O_2^-{}_{aq} + H_2O_{2aq} \rightarrow O_{2aq} + OH_{aq} + OH^-{}_{aq}$	$2.16x10^{-24}$
$O_2^-{}_{aq} + NO_{aq} \rightarrow NO_3^-{}_{aq}$	$6.0x10^{-12}$
$O_{3aq} \rightarrow O_{2aq} + O_{aq}$	$3.0x10^{-6}$
$O_{3aq} + OH^-{}_{aq} \rightarrow O_2^-{}_{aq} + HO_{2aq}$	$1.16x10^{-19}$
$N_{aq} + N_{aq} \rightarrow N_{2aq}$	$5.0x10^{-14}$
$N_{aq} + H_2O_{aq} \rightarrow NH_{aq} + OH_{aq}$	$6.93x10^{-39}$
$NH_{aq} + NO_{aq} \rightarrow N_2O_{aq} + H_{aq}$	$1.3x10^{-12}$
$NH_{aq} + O_{2aq} \rightarrow HNO_{aq} + O_{aq}$	$2.3x10^{-13}$
$NO_{aq} + NO_{aq} + O_{2aq} \rightarrow NO_{2aq} + NO_{2aq}$	$6.28x10^{-36}$
$NO_{aq} + NO_{2aq} + H_2O_{aq} \rightarrow HNO_{2aq} + HNO_{2aq}$	$5.55x10^{-34}$
$NO_{aq} + HO_{2aq} \rightarrow HNO_{3aq}$	$5.33x10^{-12}$
$NO_{aq} + HO_{2aq} \rightarrow ONOOH_{aq}$	$5.33x10^{-12}$
$NO_{aq} + O_2^-{}_{aq} \rightarrow ONOO^-{}_{aq}$	$7.14x10^{-12}$
$2\ NO_{2aq} + 2\ H_2O_{aq} \rightarrow H_3O^+{}_{aq} + NO_3^-{}_{aq} + HNO_{2aq}$	$1.26x10^{-56}$
$2\ NO_{2aq} + 3\ H_2O_{aq} \rightarrow 2\ H_3O^+{}_{aq} + NO_3^-{}_{aq} + NO_2^-{}_{aq}$	$1.30x10^{-79}$
$NO_{2aq} + OH_{aq} \rightarrow ONOOH_{aq}$	$1.99x10^{-11}$
$NO_{2aq} + H_{aq} \rightarrow HNO_{2aq}$	$1.67x10^{-11}$
$NO_2^-{}_{aq} + O_{3aq} \rightarrow NO_3^-{}_{aq} + O_{2aq}$	$5.48x10^{-16}$
$NO_{3aq} + H_2O_{aq} \rightarrow HNO_{3aq} + OH_{aq}$	$4.8x10^{-14}$
$N_2O_{3aq} + H_2O_{aq} \rightarrow HNO_{2aq} + HNO_{2aq}$	$1.93x10^{-17}$
$N_2O_{4aq} + H_2O_{aq} \rightarrow HNO_{2aq} + HNO_{3aq}$	$1.33x10^{-18}$
$N_2O_{5aq} + H_2O_{aq} \rightarrow NO_{2aq} + NO_{3aq} + H_2O_{aq}$	$1.4x10^{-19}$
$N_2O_{5aq} + H_2O_{aq} \rightarrow HNO_{3aq} + HNO_{3aq}$	$2.0x10^{-21}$
$N_2O_{5aq} + H_2O_{aq} \rightarrow ONOOH_{aq} + ONOOH_{aq}$	$2.0x10^{-21}$
$H_2O_{2aq} + NO_2^-{}_{aq} + H_3O^+{}_{aq} \rightarrow ONOOH_{aq} + H_2O_{aq} + H_2O_{aq}$	$3.04x10^{-39}$
$ONOOH_{aq} + H_2O_{aq} \rightarrow H_3O^+{}_{aq} + NO_3^-{}_{aq}$	$2.9x10^{-23}$
$ONOOH_{aq} + H_2O_{aq} \rightarrow OH_{aq} + NO_{2aq} + H_2O_{aq}$	$1.24x10^{-23}$
$HNO_{aq} + O_{2aq} \rightarrow HO_{2aq} + NO_{aq}$	$8.01x10^{-21}$
$HNO_{aq} + O_{3aq} \rightarrow O_{2aq} + HNO_{2aq}$	$9.61x10^{-15}$
$HNO_{aq} + OH_{aq} \rightarrow H_2O_{aq} + NO_{aq}$	$8.00x10^{-11}$
$O_2NO_2^-{}_{aq} \rightarrow NO_2^-{}_{aq} + O_{2aq}$	$1.0x10^{0}$
$HO_2NO_{2aq} + HNO_{2aq} \rightarrow HNO_{3aq} + HNO_{3aq}$	$1.99x10^{-20}$
$HO_2NO_{2aq} \rightarrow HNO_{2aq} + O_{2aq}$	$7.0x10^{-4}$
$HO_2NO_{2aq} \rightarrow HO_{2aq} + NO_{2aq}$	$4.6x10^{-3}$
$e^-{}_{aq} + H_2O_{aq} \rightarrow H_{aq} + OH^-{}_{aq}$	$3.04x10^{-20}$
$e^-{}_{aq} + e^-{}_{aq} + 2\ H_2O_{aq} \rightarrow H_{2aq} + 2\ OH^-{}_{aq}$	$4.096x10^{-55}$
$e^-{}_{aq} + H_{aq} + H_2O_{aq} \rightarrow H_{2aq} + OH^-{}_{aq}$	$6.4x10^{-32}$
$e^-{}_{aq} + OH_{aq} \rightarrow OH^-{}_{aq}$	$4.80x10^{-11}$
$e^-{}_{aq} + H_3O^+{}_{aq} \rightarrow H_{aq} + H_2O_{aq}$	$3.68x10^{-11}$
$e^-{}_{aq} + H_2O_{2aq} \rightarrow OH_{aq} + OH^-{}_{aq}$	$1.76x10^{-11}$
$e^-{}_{aq} + HO_2^-{}_{aq} + H_2O_{aq} \rightarrow OH_{aq} + 2\ OH^-{}_{aq}$	$8.96x10^{-33}$
$e^-{}_{aq} + O_{2aq} \rightarrow O_2^-{}_{aq}$	$3.04x10^{-11}$
$e^-{}_{aq} + H_2O_{aq} \rightarrow H_2O^-{}_{aq}$	$5.0x10^{-15}$

2. Details about the 2D model

For the 2D model we use Comsol Multiphysics™ and its built-in modules for the turbulent flow, heat transfer and transport and chemistry of the species.

a) Turbulent flow module

The transport of momentum in the gas and liquid phase is calculated using the time-independent Navier-Stokes equations for an incompressible, Newtonian fluid. The continuity equation for conservation of mass and the equation for conservation of momentum are shown in equations E.9 and E.10, respectively.

$$\rho \nabla \cdot \vec{u} = 0 \tag{E.9}$$

$$\rho(\vec{u} \,.\, \nabla \vec{u}) = \nabla[-pI + \mu(\nabla \vec{u} + (\nabla \vec{u})^T)] \tag{E.10}$$

Here, ρ is the mass density in kg.m^3, p is the pressure in Pa, μ is the dynamic viscosity and $\vec{u}$ is the fluid velocity field in m.s^{-1}. Both ρ and μ are determined by the properties of the fluid (i.e. air and water in our model).

To determine whether a flow is laminar or turbulent, the Reynolds number (Re) is calculated (equation E.11).

$$Re = \frac{\rho . U . L}{\mu} \tag{E.11}$$

Here, U is the velocity magnitude and L is the length scale, which is the diameter of the tube (i.e. of the plasma jet, i.e., 1.6 mm) in our case.

The Reynolds number for the gas flow is ca. 2200 in our case. Since this value is higher than the typical limit value of 2100[9] we consider the flow as turbulent. The turbulence effects are calculated using the standard two-equation k-ε turbulence model.[10]

b) Heat transfer module

Heat transfer is calculated with the time-dependent equation E.12 for the conservation of energy.

$$\rho \,.\, C_p\left(\frac{\partial T}{\partial t} + \vec{u} \,.\, \nabla T\right) = \nabla \,.\, (k \nabla T) + Q \tag{E.12}$$

$$Q = J_{z,H_2O} \cdot H_{vap} \tag{E.13}$$

Here, C_p is the specific heat capacity at constant pressure in J. kg^{-1}.K^{-1} and T the temperature in K. The first term at the right side is the heat transfer due to conduction, with k the thermal conductivity in W.m^{-1}.K^{-1}. Q stands for additional heat transfer introduced in the system, due to the evaporation of water from the liquid phase into the gas phase. This heat of evaporation can be calculated using equation E.13[8,11]. Here, J_{z,H_2O} is the molar flux of H_2O over the interface due to evaporation (see below) and H_{vap} represents the latent heat of evaporation for water (i.e. 2260 kJ.kg^{-1} [8]). However, when comparing with experimental results, the heat loss in the liquid is overestimated using this formula. In these experiments, we measured the temperature of the liquid during plasma treatment with a thermocouple for eight different conditions (different flow rate, gap, liquid volume). Based on these results we found that the liquid can both cool down and warm up during plasma treatment, depending on the used conditions. A low flow rate and small gap result in a slight increase in temperature of the liquid, while for a high flow rate and large gap the temperature of the liquid slightly decreases. The temperature changes are relatively small, i.e. for our conditions the maximum temperature change was 3.6 ± 0.5 K. Using E.13 for the evaporation of heat, the temperature is found to decrease by 40 K, and thus is largely overestimated. In order to compensate for this overestimation, we introduced a correction factor of 0.045 to E.13. This correction factor gives the best results on average for all the

conditions that were experimentally measured. We have chosen for one correction factor for all conditions, instead of a correction factor for each condition separately. Using this correction factor, there are still small deviations from the experimentally measured temperatures (maximum of 7 K). However, these small deviations in the liquid temperature will not affect the results significantly, because the liquid reactions are not dependent on the liquid temperature at all.

c) Transport of species and chemistry module

The transport of species in the gas and liquid phase is calculated using the time-dependent equation for conservation of mass (E.14).

$$\frac{\partial c_i}{\partial t} + \nabla . \left(- D_i \nabla c_i \right) + \vec{u} . \nabla c_i = R_i \qquad \text{(E.14)}$$

Here, c_i is the concentration of species i in mol.m^{-3} and D_i the diffusion coefficient of species i in m^2.s^{-1}. R_i is the sum of all production and loss terms of species i caused by chemical reactions, which are included in the chemistry module.

The concentrations of the species are thus dependent on diffusion, according to their diffusion constants in both gas and liquid phase (see Table S.2), and convection, determined by the velocity field calculated in the turbulent flow module, but also on the initial inlet concentrations, based on the 0D model (Table S.2) and the production and loss of species due to the gas phase and liquid phase reactions (shown in Table S.3 and S.4, respectively).

Table S.2. *Inlet concentrations adopted from the 0D model (C), diffusion constants for both gas (D_g) and liquid (D_{aq}) phase, and Henry's constants (H_i^0) and temperature correction factors (see equation E.17) (S) for every species included in the 2D model, as well as the references where the values were taken from. If a species is mentioned as reference, the value is taken the same as for this species, because no information was available.*

Species	**C**	**D_g**	**Ref**	**D_{aq}**	**Ref**	**H_i^0**	**S**	**Ref**
	cm^{-3}	10^{-5} m^2.s^{-1}		10^{-9} m^2.s^{-1}		mol.L^{-1}.atm^{-1}	K	
Ar	2.23 x 10^{19}	12.2	12					
O_2	5.51 x 10^{13}	2.10	12	2.30	13	1.3 x 10^{-3}	1500	14
N_2	2.35 x 10^{14}	2.10	12	2.60	15	6.5 x 10^{-4}	1300	14
H_2	3.19 x 10^{11}	7.78	12	1.00	13	7.8 x 10^{-4}	500	14
O	2.60 x 10^{13}	3.20	12	2.80	OH	1.3 x 10^{-3}	1500	O_2
N	5.68 x 10^{12}	2.90	12	2.80	13	6.5 x 10^{-4}	1300	N_2
H	3.11 x 10^{13}	12.2	12	1.00	13	7.8 x 10^{-4}	500	H_2
H_2O	5.63 x 10^{13}	2.30	12	2.30	16			
OH	1.93 x 10^{12}	4.00	12	2.80	13	3.0 x 10^{1}	4500	14
H_2O_2	1.49 x 10^{9}	2.00	12	1.70	13	7.1 x 10^{4}	7000	14
HO_2	2.86 x 10^{11}	2.00	12	1.70	H_2O_2	4.0 x 10^{3}	5900	14
O_3	2.01 x 10^{9}	1.50	12	1.76	17	1.2 x 10^{-2}	2700	14
NO	9.47 x 10^{11}	2.00	12	2.20	13	1.9 x 10^{-3}	1400	14
NO_2	1.27 x 10^{10}	1.70	12	1.85	13	1.2 x 10^{-2}	2500	14
N_2O	1.96 x 10^{10}	1.60	12	2.00	13	2.5 x 10^{-2}	2600	14
NO_3	2.19 x 10^{9}	0.90	12	2.50	HNO_3	2.0	2000	14
HNO	7.76 x 10^{10}	2.10	12	1.70	13	1.15 x 10^{3}		4
HNO_2	2.68 x 10^{10}	2.10	12	2.50	13	4.9 x 10^{1}	4900	14
HNO_3	8.74 x 10^{7}	2.10	12	2.50	13	2.6 x 10^{6}	8700	14
ONOOH				2.00	13	4.8 x 10^{6}		13
NH	3.61 x 10^{10}	4.00	OH	2.80	13	1.47 x 10^{3}		4
O_2(1D)	1.56 x 10^{12}	2.10	12					
O_2^-				2.30	13			

NO_2^-				1.85	[13]			
NO_3^-				2.50	[13]			
$ONOO^-$				2.00	NO_3^-			

The transport of species through the gas-liquid interface is introduced by Henry's law (E.15)[14]. The Henry's constants are introduced as temperature-dependent constants, calculated according to equation E.16 (the constants for every species are listed in Table S.2).

$$c_{i,aq} = H_i \,.\, RT \,.\, c_{i,g} \tag{E.15}$$

$$H_i = H_i^0 \,.\, exp(S \,.\, \left(\frac{1}{T} - \frac{1}{T_0}\right)) \tag{E.16}$$

Here, $c_{i,aq}$ and $c_{i,g}$ are the concentrations of species i in the liquid phase and gas phase, respectively, and H_i is the temperature-dependent Henry's constant of species i in mol.L^{-1}.atm^{-1}. H_i^0 is the Henry's constant at the standard temperature of 298.15 K, and factor S (in K) can be found in Table S.2.

As mentioned before, the evaporation of water is introduced in the model, in the heat transfer module, but also in the transport of species. Water will evaporate into the gas phase, and this value can be determined based on the vapour pressure of water (p), calculated with Antoine's law[18] (E.17).

$$\log(p) = 8.07131 - \frac{1730.63}{233.426 + T} \tag{E.17}$$

Table S.3 *Gas phase reactions and their rate coefficients implemented in the 2D model. The rate coefficient is given in the Arrhenius form: k = A x (T/300)^B x exp(-C/T), where T is the gas phase temperature. The units are s^{-1}, cm^3.s^{-1} and cm^6.s^{-1} for first, second, and third order reactions, respectively. The unit of A is the same as for k, B is dimensionless, and the unit of C and T is K. If B and/or C are not specified, their value is 0. The reactions and data for the rate coefficients are taken from the 0D model, where the gas phase chemistry was adopted from Murakami et al.[6] and from Van Gaens and Bogaerts[7]. For the last reaction, the value of the rate coefficient was calculated in the 0D model, in order to be able to implement this reaction in the 2D model (as there are no electrons in the 2D model), since it was found to be an important loss reaction of H_2O_2.*

Gas phase reactions in the 2D model	**A**	**B**	**C**
Ar + O_2(1D) ✂ Ar + O_2	3.0 x 10^{-18}		
O + NO_2 ✂ O_2 + NO	6.5 x 10^{-12}		-120.0
O + NO_3 ✂ O_2 + NO_2	1.0 x 10^{-11}		
O + OH ✂ O_2 + H	1.81 x 10^{-11}	-0.31	-177
N + NO ✂ O + N_2	8.2 x 10^{-11}		410
N + NO_2 ✂ O + N_2O	1.66 x 10^{-12}		-220
N + OH ✂ NO + H	4.70 x 10^{-11}		
NO + NO_3 ✂ 2 NO_2	1.8 x 10^{-11}		-110.0
NO_2 + H ✂ NO + OH	4.0 x 10^{-10}		340.0
NO_3 + H ✂ NO_2 + OH	5.8 x 10^{-10}		750.0
2 OH ✂ O + H_2O	4.2 x 10^{-12}		240.0
Ar + 2 O ✂ Ar + O_2(1D)	9.88 x 10^{-35}		
Ar + O + O_2 ✂ Ar + O_3	6.40 x 10^{-35}		-663
Ar + O + O_2(1D) ✂ Ar + O + O_2	1.0 x 10^{-32}		
Ar + O + NO ✂ Ar + NO_2	1.0 x 10^{-31}	-1.6	
H + O_2 + Ar ✂ HO_2 + Ar	6.09 x 10^{-32}	-0.8	
2 H + Ar ✂ H_2 + Ar	2.00 x 10^{-32}	-1	
H + HO_2 ✂ H_2 + O_2	2.06 x 10^{-11}	0.84	277
H + HO_2 ✂ 2 OH	1.66 x 10^{-10}		413
H_2 + O ✂ OH + H	1.60 x 10^{-11}		4570

$H_2 + OH \not\rightarrow H_2O + H$	9.54×10^{-13}	2	1490
$OH + NO + M \not\rightarrow HNO_2 + M$	7.40×10^{-31}	-2.4	
$OH + NO_2 + M \not\rightarrow HNO_3 + M$	4.60×10^{-29}	-5.49	1180
$OH + NO_3 \not\rightarrow HO_2 + NO_2$	2.00×10^{-11}		
$2\ OH + M \not\rightarrow H_2O_2 + M$	8.00×10^{-31}	-0.8	
$OH + HO_2 \not\rightarrow H_2O + O_2$	4.80×10^{-11}		-250
$OH + H_2O_2 \not\rightarrow H_2O + HO_2$	4.53×10^{-12}		288.9
$OH + HNO_2 \not\rightarrow H_2O + NO_2$	2.70×10^{-12}		-260
$OH + HNO_3 \not\rightarrow H_2O + NO_3$	1.50×10^{-13}		
$HO_2 + O \not\rightarrow OH + O_2$	2.71×10^{-11}		-224
$HO_2 + O_2(1D) \not\rightarrow OH + O_2 + O$	1.66×10^{-11}		
$HO_2 + N \not\rightarrow OH + NO$	2.20×10^{-11}		
$HO_2 + NO + Ar \not\rightarrow HNO_3 + Ar$	5.60×10^{-33}		
$H_2O_2 + O \not\rightarrow HO_2 + OH$	1.79×10^{-13}	2.92	1394
$H_2O_2 + O \not\rightarrow H_2O + O_2$	1.45×10^{-15}		
$HNO_2 + O \not\rightarrow OH + NO_2$	2.00×10^{-11}		3000
$HNO_3 + O \not\rightarrow OH + NO_3$	3.00×10^{-17}		
$O + NO_2 + Ar \not\rightarrow NO_3 + Ar$	9.00×10^{-32}	-2	
$H + NO + Ar \not\rightarrow HNO + Ar$	1.22×10^{-31}	-1.17	212
$HO_2 + NO \not\rightarrow HNO + O_2$	9.10×10^{-19}		-2819
$NH + O \not\rightarrow H + NO$	1.16×10^{-10}		
$NH + O \not\rightarrow OH + N$	1.16×10^{-10}		
$HNO + O \not\rightarrow OH + NO$	6.00×10^{-11}		
$O_3 + H \not\rightarrow O_2 + OH$	2.71×10^{-11}	0.75	
$N + NO_3 \not\rightarrow NO + NO_2$	3.0×10^{-12}		
$H + HO_2 \not\rightarrow H_2O + O$	5.00×10^{-11}		866
$H + H_2O_2 \not\rightarrow H_2O + OH$	4.00×10^{-11}		2000
$2\ O + M \not\rightarrow O_2(1D) + M$	6.93×10^{-35}	-0.63	
$H + N + Ar \not\rightarrow NH + Ar$	5.00×10^{-32}		
$H + NH \not\rightarrow H_2 + N$	1.70×10^{-11}		
$H + HNO \not\rightarrow H_2 + NO$	3.00×10^{-11}		500
$OH + NH \not\rightarrow H_2 + NO$	4.00×10^{-11}		
$OH + NH \not\rightarrow HNO + H$	4.00×10^{-11}		
$OH + HNO \not\rightarrow H_2O + NO$	8.00×10^{-11}		500
$HO_2 + N \not\rightarrow NH + O_2$	1.70×10^{-13}		
$H_2O_2 + e \not\rightarrow H_2O + O^-$	$k = 8.9854 \times 10^{-13}\ m^3.s^{-1}$		

Table S.4. *Liquid phase reactions and their rate coefficients implemented in the 2D model. The unit of the rate coefficient is s^{-1}, $m^3.mol^{-1}.s^{-1}$, $m^6.mol^{-2}.s^{-1}$, $m^9.mol^{-3}.s^{-1}$, $m^{12}.mol^{-4}.s^{-1}$, and $m^{15}.mol^{-5}.s^{-1}$ for first, second, third, fourth, and fifth order reactions, respectively. The reactions and rate coefficients are taken from the 0D model, where the liquid chemistry was adopted from Lietz and Kushner.[4] The reaction numbers are used in Tables 3 and 4 and Figure 9 of the main paper.*

No.	Liquid phase reactions in the 2D model	k
1	$ONOOH + H_2O \rightarrow H_3O^+ + ONOO^-$	5.0×10^{-15}
2	$HO_2 + H_2O \rightarrow H_3O+ + O_2^-$	1.43×10^{-17}
3	$HNO_2 + H_2O \rightarrow H_3O^+ + NO_2^-$	5.0×10^{-15}
4	$HNO_3 + H_2O \rightarrow H_3O^+ + NO_3^-$	3.0×10^{-18}
5	$OH + H \not\rightarrow H_2O$	3.0×10^{-11}
6	$2\ OH \not\rightarrow H_2O_2$	1.7×10^{-11}
7	$OH + H_2 \not\rightarrow H + H_2O$	6.0×10^{-14}
8	$OH + HO_2 \not\rightarrow O_2 + H_2O$	2.0×10^{-11}
9	$OH + H_2O_2 \not\rightarrow HO_2 + H_2O$	1.0×10^{-13}
10	$OH + O_2^- \not\rightarrow O_2 + OH^-$	1.5×10^{-11}
11	$H + H_2O \not\rightarrow H_2 + OH$	1.5×10^{-21}

12	$2\ H \not\rightarrow H_2$	1.5×10^{-11}
13	$H + HO_2 \not\rightarrow H_2O_2$	3.0×10^{-11}
14	$H + H_2O_2 \not\rightarrow H_2O + OH$	1.5×10^{-13}
15	$H_2 + H_2O_2 \not\rightarrow H + OH + H_2O$	1.0×10^{-14}
16	$O + O_2 \not\rightarrow O_3$	5.0×10^{-12}
17	$O_2^- + HO_2 + H_2O \not\rightarrow O_2 + H_2O_2 + OH^-$	2.68×10^{-34}
18	$O_2^- + H_2O_2 \not\rightarrow O_2 + OH + OH^-$	2.16×10^{-22}
19	$O_3 \not\rightarrow O_2 + O$	3.0×10^{-6}
20	$O_3 + OH^- \not\rightarrow O_2^- + HO_2$	1.16×10^{-19}
21	$2\ N \not\rightarrow N_2$	5.0×10^{-14}
22	$NH + NO \not\rightarrow N_2O + H$	1.3×10^{-12}
23	$NH + O_2 \not\rightarrow HNO + O$	2.3×10^{-13}
24	$OH + NO_2^- \not\rightarrow OH^- + NO_2$	1.7×10^{-11}
25	$H + NO_2^- \not\rightarrow NO + OH^-$	2.0×10^{-12}
26	$O_2^- + NO \not\rightarrow NO_3^-$	6.0×10^{-12}
27	$2\ NO_2 + 2\ H_2O \not\rightarrow H_3O^+ + NO_3^- + HNO_2$	1.26×10^{-56}
28	$2\ NO_2 + 3\ H_2O \not\rightarrow 2\ H_3O^+ + NO_3^- + NO_2^-$	1.30×10^{-79}
29	$2\ NO + O_2 \not\rightarrow 2\ NO_2$	6.28×10^{-36}
30	$NO + NO_2 + H_2O \not\rightarrow 2\ HNO_2$	5.55×10^{-34}
31	$NO + HO_2 \not\rightarrow HNO_3$	5.33×10^{-12}
32	$NO_2 + H \not\rightarrow HNO_2$	1.67×10^{-11}
33	$OH + NO \not\rightarrow HNO_2$	3.3×10^{-11}
34	$OH + NO_2 \not\rightarrow HNO_3$	2.0×10^{-11}
35	$OH + HNO_3 \not\rightarrow NO_3 + H_2O$	2.17×10^{-13}
36	$H + HNO_2 \not\rightarrow NO + H_2O$	7.5×10^{-13}
37	$NO_2^- + O_3 \not\rightarrow NO_3^- + O_2$	6.15×10^{-16}
38	$NO + HO_2 \not\rightarrow ONOOH$	5.33×10^{-12}
39	$NO_2 + OH \not\rightarrow ONOOH$	1.99×10^{-11}
40	$H_2O_2 + NO_2^- + H_3O^+ \not\rightarrow ONOOH + 2\ H_2O$	3.04×10^{-39}
41	$ONOOH + H_2O \not\rightarrow H_3O^+ + NO_3^-$	2.9×10^{-23}
42	$ONOOH + H_2O \not\rightarrow OH + NO_2 + H_2O$	1.24×10^{-23}
43	$NO + O_2^- \not\rightarrow ONOO^-$	7.14×10^{-12}
44	$HNO + O_2 \not\rightarrow HO_2 + NO$	8.01×10^{-21}
45	$HNO + O_3 \not\rightarrow O_2 + HNO_2$	9.61×10^{-15}
46	$HNO + OH \not\rightarrow H_2O + NO$	8.00×10^{-11}
47	$OH + N_2O \not\rightarrow HNO + NO$	3.8×10^{-17}
48	$NO_2^- + N_2O \not\rightarrow NO_3^- + N_2$	5.0×10^{-13}
49	$2\ HNO_2 \not\rightarrow NO + NO_2 + H_2O$	2.23×10^{-17}
50	$NO_3 + OH^- \not\rightarrow OH + NO_3^-$	1.32×10^{-13}
51	$ONOO^- \not\rightarrow NO + O_2^-$	2.00×10^{-2}
52	$HO_2 + HO_2 \not\rightarrow O_2 + H_2O_2$	1.38×10^{-12}

3. Validation of the gas phase densities

To verify whether our reaction kinetics model is correct, we performed simulations to mimic the conditions of Schmidt-Bleker et al.[5] and Hansen et al.[19]. Indeed, the densities of some species presented in our paper, i.e., O_3 and NO_2, are one or two orders of magnitude lower than in Schmidt-Bleker et al.[5] and Hansen et al.[19], and we want to elucidate the underlying reason for this discrepancy. As in both papers a shielding gas device was used, this was also added in our model, as shown in Figure S.5. The geometry of the device in Reuter et al.[20] is modelled, which is referenced by Schmidt-Bleker et al.[5]. The tube supplying the shielding gas was ignored to keep the rotational symmetry of the

system, and instead the inlet was placed at the top of the shielding gas device. Dry synthetic air (20% O_2 and 80% N_2) was used as the shielding gas at a flow rate of 5 slm.

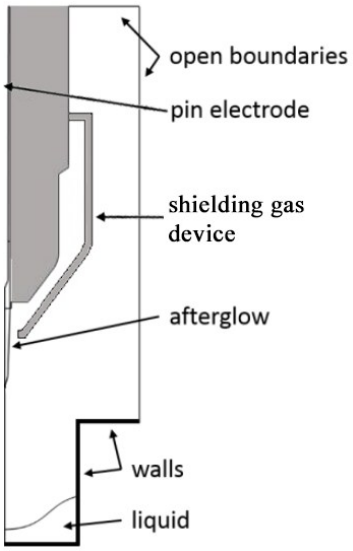

Figure S.5. *Geometry of the 2D model after addition of the shielding gas device.*

We followed the same computational flowchart as for our other simulations: a 2D simulation with no chemistry was performed, followed by a 0D chemical kinetics simulation (see Figure 2 in the main paper).

From Figure 6 in the main paper, it is clear that the air density inside the well remains high during the plasma treatment when using a shielding gas, whereas without shielding gas the air density is almost zero inside the well after a few seconds (Figure 5 in the main paper). Moreover, in the center of the effluent, the O_2 and N_2 densities are two orders of magnitude higher when a shielding gas is used, because of the constant supply of air.

This is important since the concentration of ambient air species determines the amount of RONS that are produced. O_3 is mainly produced via the reaction:

$$O_2 + O \rightarrow O_3$$

Thus, we would expect a higher ozone concentration for a higher presence of O_2. The results of the 0D-model, with and without shielding gas, are shown in Figure S.6.

It can be seen that even though the ozone density at the end of the afterglow (position 1.5 cm), which is the value used as input in the 2D model, is almost the same with or without the gas shield, the density has become almost two orders of magnitude higher with gas shield compared to without gas shield by the time the gas flow reaches the liquid surface (8.8×10^{12} cm^{-3} vs 2.6×10^{11} cm^{-3}). We could not calculate the ozone density in the far field with our 2D model when a shielding gas device is used, since this would take several months, as was the case for the calculations without gas shield. However, we can draw some conclusions based on Figure S.6. Because the ozone density in the 2D-simulation reaches a maximum of 1.3×10^{13} cm^{-3}, this means that the density still rises quite a bit after the gas flow has reached the liquid surface. Since the ozone density is almost two orders of magnitude higher with a shielding gas when the gas flow reaches the liquid surface, we expect the same for the density in the far field. This would put the O_3 density around the values measured in Schmidt-Bleker et al.[5] and

Hansen et al.[19]. The discrepancy between our work and the results of Schmidt-Bleker et al.[5] and Hansen et al.[19] for the O_3 density, as mentioned above and in the main paper, can thus be explained by the fact that in our work no shielding gas was used. Of course we cannot directly compare the values for the far field without performing a full 2D-simulation of the system with gas shield, but as the latter takes several months, the above reasoning can also give useful insights.

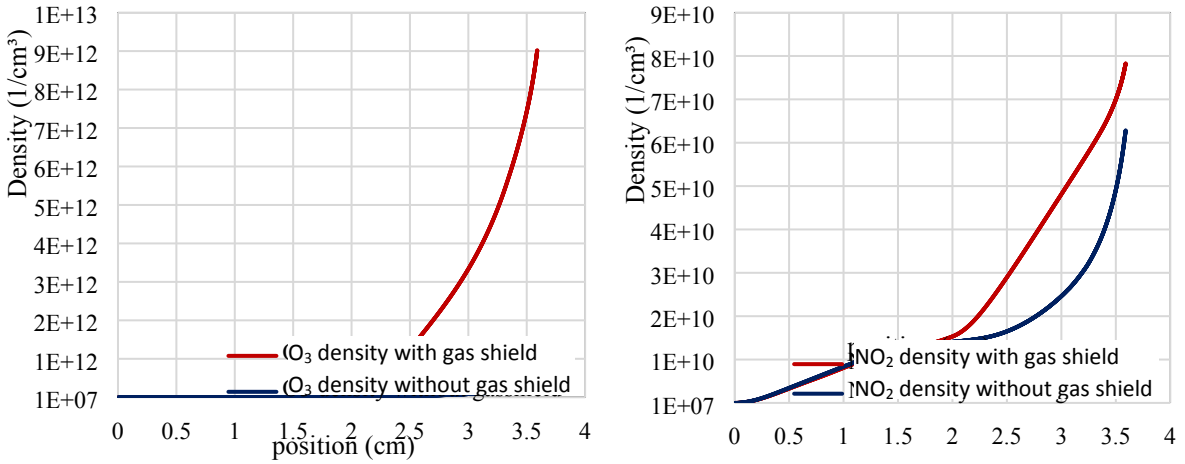

Figure S.6. *Density of O_3 (left) and NO_2 (right) as a function of position, with and without gas shield. Position 0 cm corresponds to the end of the pin electrode, position 1.5 cm is the end of the afterglow and position 3.5 cm is the liquid surface.*

The explanation given above for the discrepancy between the ozone density in our work and the work of Schmidt-Bleker et al.[5] and Hansen et al.[19] does however not apply for the second main species discussed in Schmidt-Bleker et al.[5] and Hansen et al.[19]: NO_2. In our work the density of NO_2 inside the vortex in the well reaches a value around $2\text{x}10^{11}$ cm^{-3}, while in Hansen et al.[19] this density is measured to be around $2\text{x}10^{13}$ cm^{-3}. The value in Schmidt-Bleker et al.[5], where no liquid phase was included, cannot be compared since in Hansen et al.[19] it was proven that a liquid surface has a large effect on the NO_2 density (while not having a significant effect on the O_3 density). Figure S.6 illustrates that the gas shield has a minor effect on the NO_2 density compared to the ozone density. However, we see other explanations for this discrepancy.

First of all, our model reveals that a large amount of NO_2 in the gas phase is actually formed in the liquid phase, mainly through reaction

$$OH + NO_2^- \rightarrow OH^- + NO_2$$

Subsequently, it diffuses to the gas phase due to its small Henry's constant. In Hansen et al.[19] however the gap between the plasma jet and the liquid surface is much smaller than in our model, which may affect the concentration of short lived species, like OH, that are able to diffuse into the liquid, and thus the NO_2 production.

Another possible explanation is related to the impurities in the feed gas. In our simulations with gas shield, the concentrations of the impurities in the feed gas were kept the same as in our previous simulations without gas shield (O_2 = 1 ppm, N_2 = 4 ppm and H_2O = 3 ppm). These impurities, however, can have a large influence on the RONS production, as was also discussed in Schmidt-Bleker et al.[5]. Only the impurity concentration of H_2O is given in Schmidt-Bleker et al.[5] (5 ppm) but to obtain a full picture of the influence of the impurities, the concentrations of O_2 and N_2 were both estimated to be

4 ppm (= 9.8x10^{13} cm^{-3}) from Figure 5 in Schmidt-Bleker et al.[5] Hence, we also performed 0D simulations with these values, and the results indeed reveal that the difference in impurity values can further explain the discrepancies in species densities: with the impurity concentrations estimated from Schmidt-Bleker et al.[5] the densities of O_3 and NO_2 near the liquid surface are calculated to be 1.67x10^{13} cm^{-3} and 1.51x10^{11} cm^{-3}, respectively, compared to 8.80x10^{12} cm^{-3} and 7.68x10^{10} cm^{-3} in our simulations with the initial impurities (O_2 = 1 ppm, N_2 = 4 ppm and H_2O = 3 ppm), as seen in Figure S.6. However, since the O_2 and N_2 impurities were merely estimated for this simulation, these values cannot actually be compared with certainty; they only indicate that the impurity concentrations also largely affect the RONS production.

4. Study on the underestimation of species concentrations due to the static liquid interface

To verify our hypothesis that the underestimation of the species concentrations in the liquid is indeed due to the use of a static instead of a turbulent liquid surface in the model, we performed additional simulations, mimicking the experiments of Winter et al.[21] where H_2O_2-containing argon gas was applied to a liquid surface without plasma ignition. We built the geometry used in Winter et al.[21] in our model (see Figure S.7) and tried to reveal whether the transport of gas phase species into the liquid is indeed underestimated.

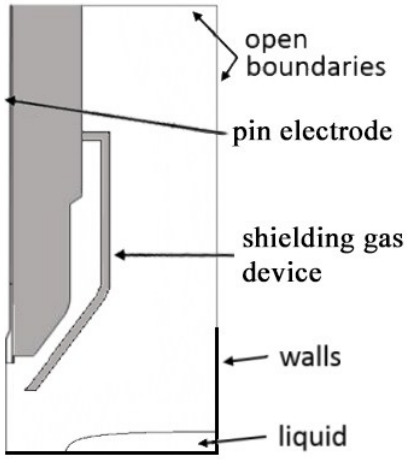

Figure S.7. *New geometry of the 2D model for investigating the transport over the gas-liquid interface.*

In the geometry used by Winter et al.[21], the kINPen is positioned over a Petri dish (60 mm diameter, TPP) with an inner diameter of 53 mm. The Petri dish is filled with 5 ml water. The gap between the jet and the liquid surface (in rest) was 0.9 mm. The dimple in the liquid surface was not visualized experimentally, but instead based on the depth and width of the dimple reported in our paper. The gas shield device was modelled based on Schmidt-Bleker et al.[22], which is cited by Winter et al.[21]. Since there is no plasma ignition, there is also no afterglow in this model. The feed gas was argon with a certain amount of H_2O_2. Two different 2D simulations were performed, with an H_2O_2 density of either 1.23x10^{14} cm^{-3} or 6.16x10^{13} cm^{-3}, corresponding to 5 ppm and 2.5 ppm, respectively, i.e. two of the values used by Winter et al.[21] (see Figure 8 of their paper). These simulations were performed for 100 seconds treatment, and the H_2O_2-concentration in the liquid was calculated at times 40 s, 60 s and 80 s, to be able to compare them with the measured results from Winter et al.[21]. If the turbulent moving of the liquid surface is indeed important, we expect an underestimation of the calculated H_2O_2

concentration in the liquid. The comparison between calculated and measured results is shown in Figure S.8.

It can be seen that the calculated H_2O_2 concentration is indeed underestimated, and the discrepancy becomes larger upon increasing treatment time. This means that the gas-liquid interface is in fact not yet modelled 100% correctly, most probably due to the turbulent movement of the liquid surface. Indeed, the reason cannot be the chemistry, as it is absent in this case. The underestimation is however less pronounced than in our model with the well plate, where the H_2O_2-concentration was 11 times lower than experimentally measured, while in this case the calculated concentration is at maximum only 2.3 times too low (at 80 seconds treatment with 2.5 ppm H_2O_2). There are two possible explanations for this. First, the Petri dish used in the experiments by Winter et al.[21] is much larger than the wells used in our study, and the water surface might thus move less turbulently, more approaching a static interface like in the model. This would mean that our model can provide a "more correct" description of the gas-liquid interface for the Petri dish than for the well plate. A second explanation is that the underestimation of the species concentrations in the liquid is not only due to the static interface in the model, but in addition also due to some underestimation of the gas phase concentrations of certain species.

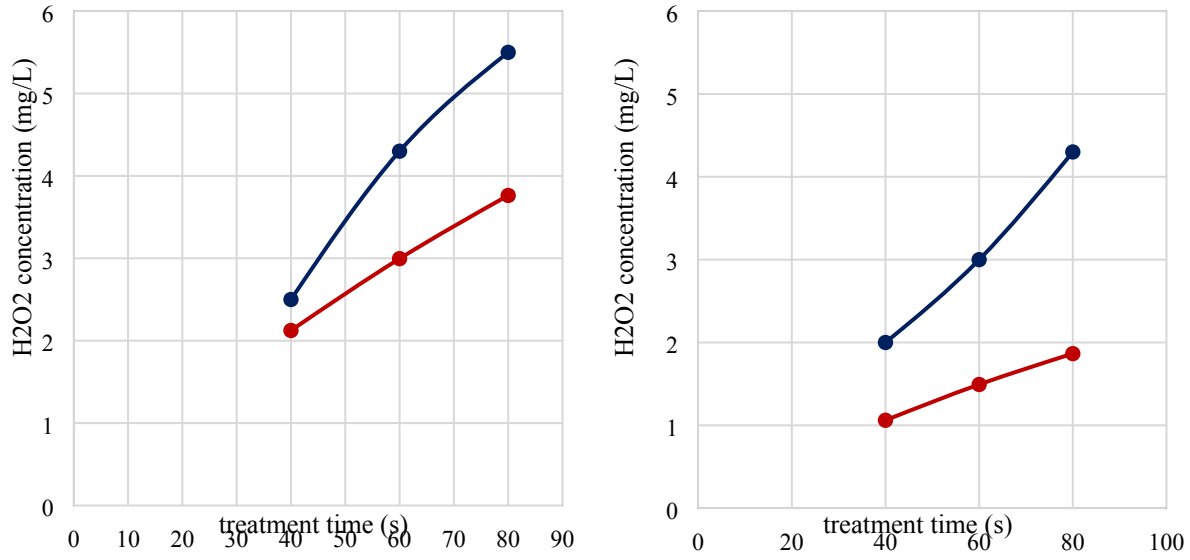

Figure S.8. *Calculated and measured H_2O_2 concentrations in the liquid as a function of treatment time, for two different H_2O_2 concentrations in the argon gas, i.e., 5 ppm (left) and 2.5 ppm (right), for the setup described by Winter et al.[21] The experimental results obtained by Winter et al. are given by the blue data points, while the computational results obtained with our model are shown with the red data points. It can be seen that our model indeed underestimates the amount of H_2O_2 that dissolves from the gas phase into the liquid phase, which can be attributed to the use of a static interface.*

5. References

(1) Pancheshnyi, S.; Eismann, B.; Hagelaar, G. J. M.; Pitchford, L. C. ZDPlasKIN: A New Tool for Plasmachemical Simulations. **2008**.

(2) Hagelaar, G. J. M.; L.C., P. Solving the Boltzmann Equation to Obtain Electron Transport Coefficients and Rate Coefficients for Fluid Models. *Plasma Sources Sci. Technol.* **2005**, *14*, 722–733.

(3) Lieberman, M. A.; Lichtenberg, A. J. *Principles of Plasma Discharges and Materials Processing (second Edition)*; Wiley-Interscience, 2005.
(4) Lietz, A. M.; Kushner, M. J. Air Plasma Treatment of Liquid Covered Tissue: Long Timescale Chemistry. *J. Phys. D. Appl. Phys.* **2016**, *49*, 425204.
(5) Schmidt-Bleker, A.; Winter, J.; Bösel, A.; Reuter, S.; Weltmann, K.-D. On the Plasma Chemistry of a Cold Atmospheric Argon Plasma Jet with Shielding Gas Device. *Plasma Sources Sci. Technol.* **2016**, *25*, 015005.
(6) Murakami, T.; Niemi, K.; Gans, T.; Connell, D. O. Chemical Kinetics and Reactive Species in Atmospheric Pressure Helium – Oxygen Plasmas with Humid-Air Impurities. *Plasma Sources Sci. Technol.* **2013**, *22*, 1–29.
(7) Van Gaens, W.; Bogaerts, a. Kinetic Modelling for an Atmospheric Pressure Argon Plasma Jet in Humid Air. *J. Phys. D. Appl. Phys.* **2013**, *46*, 275201.
(8) Verlackt, C. C. W.; Van Boxem, W.; Bogaerts, A. Transport and Accumulation of Plasma Generated Species in Aqueous Solution. *Phys. Chem. Chem. Phys.* **2018**, *20*, 6845–6859.
(9) Trinh, K. T. On The Critical Reynolds Number For Transition From Laminar To Turbulent Flow. *arXiv:1007.0810* **2010**.
(10) Wilcox, D. C. *Turbulence Modelling for CFD*; DCW Industries, Inc., 1993.
(11) Lindsay, A.; Anderson, C.; Slikboer, E.; Shannon, S.; Graves, D. Momentum, Heat, and Neutral Mass Transport in Convective Atmospheric Pressure Plasma-Liquid Systems and Implications for Aqueous Targets. *J. Phys. D. Appl. Phys.* **2015**, *48*, 424007.
(12) Sakiyama, Y.; Graves, D. B.; Chang, H.-W.; Shimizu, T.; Morfill, G. E. Plasma Chemistry Model of Surface Microdischarge in Humid Air and Dynamics of Reactive Neutral Species. *J. Phys. D. Appl. Phys.* **2012**, *45*, 425201.
(13) Lindsay, A.; Anderson, C.; Slikboer, E.; Shannon, S.; Graves, D. Momentum, Heat, and Neutral Mass Transport in Convective Atmospheric Pressure Plasma-Liquid Systems and Implications for Aqueous Targets. *J. Phys. D. Appl. Phys.* **2015**, *48*, 424007.
(14) Sander, R. Compilation of Henry ' S Law Constants for Inorganic and Organic Species of Potential Importance in Environmental Chemistry. *Database* **1999**, *20*, 107.
(15) Wise, D. L.; Houghton, G. Diffusion Coefficients of Neon, Krypton, Xenon, Carbon Monoxide and Nitric Oxide in Water at 10–60°C. *Chem. Eng. Sci.* **1968**, *23*, 1211–1216.
(16) Holz, M.; Heil, S. R.; Sacco, A. Temperature-Dependent Self-Diffusion Coefficients of Water and Six Selected Molecular Liquids for Calibration in Accurate 1H NMR PFG Measurements. *Phys. Chem. Chem. Phys.* **2000**, *2*, 4740–4742.
(17) Johnson, P. N.; Davis, R. a. Diffusivity of Ozone in Water. *J. Chem. Eng. Data* **1996**, *41*, 1485–1487.
(18) Antoine, M. C. Tensions Des Vapeurs: Nouvelle Relation Entre Les Tensions et Les Tempèratures. *Comptes Rendus des Séances l'Académie des Sci.* **1888**, *107*, 836–837.
(19) Hansen, L.; Schmidt-Bleker, A.; Bansemer, R.; Kersten, H.; Weltmann, K.-D.; Reuter, S. Influence of a Liquid Surface on the NOx Production of a Cold Atmospheric Pressure Plasma Jet. *J. Phys. D Appl. Phys* **2018**, *51*, 474002.
(20) Reuter, S.; Winter, J.; Schmidt-Bleker, A.; Tresp, H.; Hammer, M.; Weltmann, K.-D. Controlling the Ambient Air Affected Reactive Species Composition in the Effluent of an Argon Plasma Jet. *IEEE Trans. Plasma Sci.* **2012**, *40*, 2788–2794.
(21) Winter, J.; Tresp, H.; Hammer, M. U.; Iseni, S.; Kupsch, S.; Schmidt-Bleker, A.; Wende, K.; Dünnbier, M.; Masur, K.; Weltmann, K.-D.; Reuter, S. Tracking Plasma Generated H_2O_2 from Gas into Liquid Phase and Revealing Its Dominant Impact on Human Skin Cells. *J. Phys. D Appl. Phys* **2014**, *47*, 285401.
(22) Schmidt-Bleker, A.; Winter, J.; Iseni, S.; Dünnbier, M.; Weltmann, K.-D.; Reuter, S. Reactive Species Output of a Plasma Jet with a Shielding Gas Device - Combination of FTIR Absorption Spectroscopy and Gas Phase Modelling. *J. Phys. D Appl. Phys* **2014**, *47*, 145201.